

Experimental study of initial condition dependence on turbulent mixing in shock-accelerated Richtmyer–Meshkov fluid layers

S. Balasubramanian^{*†}, G.C. Orlicz and K.P. Prestridge

Physics Division, Los Alamos National Laboratory, Los Alamos, NM 87545, USA

(Received 26 October 2012; final version received 31 March 2013)

Experimental evidence is needed to verify the hypothesis that the memory of initial conditions is retained at late times in variable density flows. If true, this presents an opportunity to “design” and “control” late-time turbulence, with an improved understanding in the prediction of inertial confinement fusion and other general fluid mixing processes. In this communication, an experimental and theoretical study on the effects of initial condition parameters, namely, the amplitude δ_0 and wavenumber κ_0 ($\kappa_0 = \frac{2\pi}{\lambda_0}$, where λ_0 is the initial wavelength) of perturbations, on late-time turbulence and mixing in shock-driven Richtmyer–Meshkov (R-M) unstable fluid layers in a 2D plane is presented. Single and multi-mode membrane-free initial conditions in the form of a gas curtain having a light-heavy-light configuration (air-SF₆-air) with an Atwood number of $A = 0.57$ were used in our experiments. A planar shock wave with a shock Mach number $M = 1.21$ drives the R-M instability, and the evolution of this instability after incident shock is captured using high resolution simultaneous planar laser induced fluorescence (PLIF) and particle image velocimetry (PIV) diagnostics. Time evolution of statistics such as amplitude of the mixing layer, 2D turbulent kinetic energy, Reynolds number, rms of velocity fluctuations, probability density functions, and density-specific volume correlation were observed to quantify the amount of mixing and understand the nature of turbulence in this flow. Based on these results, it was found that the R-M mixing layer is asymmetric and non-Boussinesq. There is a correlation between initial condition parameters and large-scale, and small-scale mixing at late times, indicating an initial condition dependence on R-M mixing.

Keywords: initial conditions; Richtmyer–Meshkov instability; turbulent mixing

1. Introduction

The Richtmyer–Meshkov (R-M) instability is produced when a shock wave interacts with an interface separating two gases of varying density. During this process, vorticity is deposited at the interface by means of baroclinic torque ($\nabla p \times \nabla \rho$) caused by the misalignment of the pressure gradient of the shock and the density gradient at the initial conditions [1,2]. The rotational flow associated with this vorticity causes the interface to distort strongly in areas of maximum misalignment, forming flow structures comprised of bubbles of light fluid and spikes of heavy fluid. The R-M instability can be thought of as the impulsive limit of a Rayleigh–Taylor (R-T) instability [3]. The analysis of [1] revealed that small perturbations in the initial interface grow linearly with time, and other work such as [4] suggests that even

[†]Current address: Department of Mechanical Engineering, Indian Institute of Technology, Bombay, Maharashtra 400076, India.

^{*}Corresponding author. Email: sridharb@iitb.ac.in

when the perturbation is nonlinearly saturated, the growth continues to be linear in time. The physics of R-M instability has important implications in inertial confinement fusion, where a spherical capsule containing solid Deuterium–Tritium (D-T) and an inner space filled with gaseous D-T is compressed using powerful lasers [e.g., 5–7]. The imploding shock wave interacts with a variable density field caused by the large density difference between the solid and gaseous D-T, resulting in the R-M instability and growth of initially present small-scale random perturbations. During the implosion, R-M instability triggers turbulent mixing, which has the dual effect of diluting and cooling the fuel, reducing the efficiency of the reaction [8] and making it important to understand this mechanism. Other applications of this work include astrophysical phenomena, from supernovae to the dynamics of interstellar media, combustion processes, and mixing in scram jet engines and physics of ejecta [see 9–12]. In variable density flows, the density interface consists of random perturbations arising from surface roughness, machining grooves, or often an uneven fluid interface that initially grows in a laminar, orderly manner, and later becomes turbulent and nonlinear, thereby greatly enhancing the mixing of the two fluids. The gradients in the initial conditions strongly impact the energy deposited in the interface when a shock wave passes through it, and hence it is critical to quantify the initial condition dependence on flow mixing. The primary focus of this paper is to quantitatively study the influence of initial conditions on the development of a turbulent mixing layer due to R-M instability.

1.1. Background and motivation for the present study

In the past four decades, the growth and mixing characteristics of Richtmyer–Meshkov instability have been studied experimentally, theoretically, and numerically by various research groups [e.g., 13–36], yet some issues remain. For example, experimental diagnostics have not been able to accurately measure turbulence statistics until recently [37], so the exact nature of turbulence and mixing behavior over time under different flow conditions has been unknown. Moreover, no turbulence quantities have been experimentally measured in singly shocked R-M flows, and this information is important for theoretical and numerical validation of unsteady flows.

1.1.1. Theoretical work

Linear theory has been applied to study the growth of the mixing layer in R-M flows. For positive post-shock Atwood number ($A^+ > 0$) the growth can be represented as

$$\frac{d\delta}{dt} = A^+ \Delta U \kappa \delta_0^+, \quad (1)$$

where ΔU is the advection velocity, κ is the wavenumber of perturbations at the interface, and δ_0^+ is the post-shock amplitude of the perturbations. In Equation (1), the post-shock Atwood number and shock amplitude are used to capture shock compression effects. Later it was found that Equation (1) is applicable for pre-shock Atwood numbers $A > 0$. For $A < 0$, the growth rate depends on the average of the pre-shock amplitude (δ_0) and post-shock amplitude (δ_0^+), namely, [38]

$$\frac{d\delta}{dt} = A \Delta U \kappa \left(\frac{\delta_0^+ + \delta_0}{2} \right). \quad (2)$$

The linear theory proposed by [1] is limited to application at small amplitudes ($\kappa\delta_0 \ll 1$) and when the growth rate is small. It is also limited to the regime of small compressions, when the incident Mach number is near unity or the adiabatic indices are large. The theory loses accuracy for strong shocks when the densities or adiabatic indices differ substantially. Another analytical model was proposed by [39], which is based on the assumption that the vorticity created by the initial shock interaction evolves into a row of line vortices. This model was validated experimentally for single-mode perturbations [40]. An exact solution in the linear regime was given by Wouchuk and Nishihara [41]. Despite these theoretical efforts, due to the nonlinearity of shock-driven mixing, experiments with accurately measured initial conditions and temporally and spatially resolved mixing parameters are needed to help guide our understanding of these flows.

1.1.2. *Experimental work*

In experiments, to study R-M instability with or without reshock, an initial interface can be created either using membranes [17,18,42], or without membranes [23,30,43,44]. Although a variety of initial conditions can be used in experiments with membranes, small pieces of wire and diaphragm contaminate the flow field, causing unknown effects to the flow as well as interfering with optical diagnostics. Experiments with membrane-free initial conditions allow for high resolution measurements, but the interface is diffuse, and repeatability and characterization of initial conditions is difficult. Thus, experimental measurements in R-M flows, especially quantitative data, are very difficult, most notably in the cases involving inertial confinement fusion and astrophysical phenomena.

1.1.3. *Numerical work*

Due to the difficulties associated with theoretical and experimental study of R-M flows, an understanding of the underlying flow physics relies on insights gained through modeling and numerical simulations [see 31,45–48]. The evolution of R-M instability with single-mode initial conditions has been studied extensively, and recently some progress has been made on understanding the effects of the multi-mode nature of perturbations on R-M growth and mixing [49–52]. However, for accurate modeling of such complex flows, experimental measurements are necessary for the verification and validation of the numerical models. Hence, for a complete understanding of the physics of unsteady variable density mixing, it is important to approach the problem from all the three aspects, namely theoretical modeling, experimental measurements, and numerical modeling.

1.2. *Initial condition effects*

Historically it was thought that both R-T and R-M turbulence reach an isotropic state at late times and the flows become independent of the initial perturbations and are controlled only by the local small scales present in the flow [26,53]. However, recently there is a growing body of fundamental research that indicates only some turbulent flows are truly self-similar, and one may have to consider the influence of initial conditions on late-time flow development [see 15,54,55]. A number of studies, mostly computational, have focused on the influence of initial conditions on R-T instability [16,55,56] and R-M instability [11,31,51,57]. The lack of experimental evidence of the effect of initial conditions on late time turbulent mixing has been a bane to the verification and validation of various 2D and 3D numerical models. The difficulty in diagnosing turbulent mixing quantities in

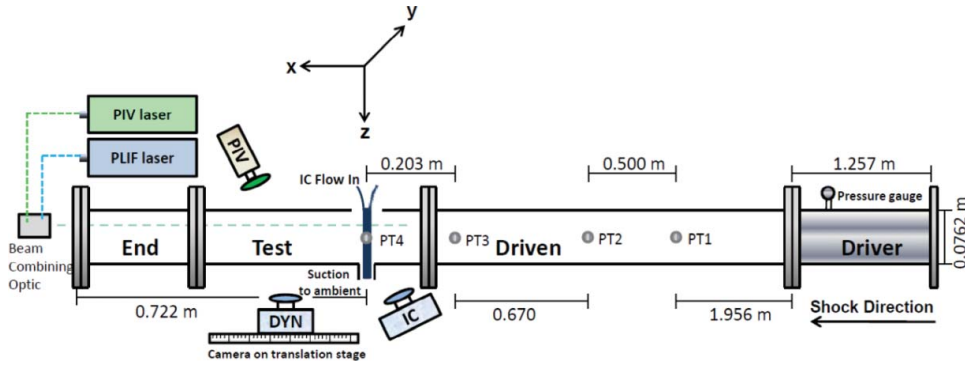


Figure 1. Schematic of the horizontal shock tube facility at Los Alamos National Laboratory. There are four pressure transducers (PT) to measure the shock speed, and lasers and cameras to perform PLIF and PIV measurements.

extreme conditions, such as a shock driven unsteady flow, makes experimental observation a challenging task, and there are only a handful of experimental results indicating a weak initial condition dependence on late time mixing in R-M flows both in the absence and presence of reshock [42,44,58,59]. In order to understand the effects of initial conditions on the late-time R-M mixing and turbulence, and to improve our methods for modeling unsteady turbulence, it is of utmost importance to experimentally measure the evolution of multiple turbulence statistics. The scope of this paper is to study the impact of different initial configurations on turbulent kinetic energy, velocity fluctuations, and other turbulence quantities. The rest of the paper is organized as follows: Section 2 presents the experimental setup and initial conditions characterization. Section 3 describes the single shock experiments using different initial condition configurations followed by results of turbulent quantities measured. The conclusions of this study are presented in Section 4.

2. Experimental setup and instrumentation

In this section, the details of the experimental facility along with the description of our high resolution diagnostics used for measurements and the characteristics of membrane-free stable initial conditions are given.

2.1. LANL horizontal gas shock tube facility

The experiments were carried out in the Horizontal Shock Tube facility at Los Alamos National Laboratory shown in Figure 1. In order to generate a shock wave, the driver section is pressurized using nitrogen as the driver gas. Once the desired pressure is reached, the diaphragm is ruptured with blades to send a shock wave downstream. For the reported experiments, a Mach $M = 1.21$ shock wave is generated within a 7.62×7.62 cm square cross-section tube spanning a total length of approximately 5.31 m [for more information on the experimental setup, see 35,43]. The shock wave travels a distance of $x \approx 3.3$ m before entering a 45 cm long test section. The initial condition in the form of a gas curtain is created inside this test section. To form the gas curtain, a mixture of SF_6 and acetone is flowed into a settling chamber. The mixture then flows into the test section through a

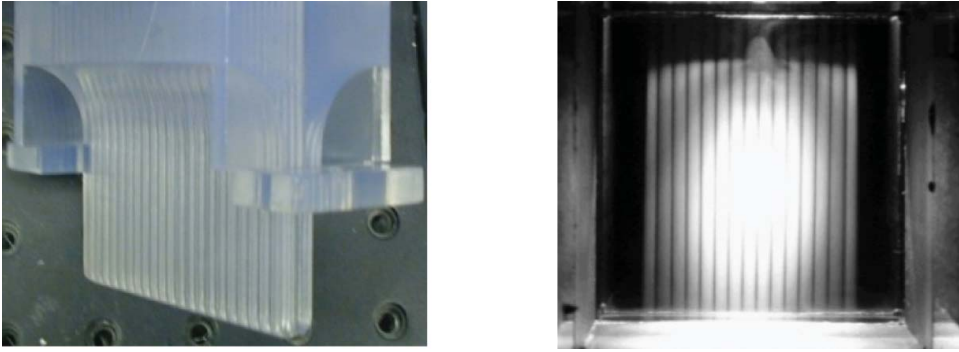


Figure 2. (left) A sample image of the nozzle configuration (manufactured using stereo-lithography) used to create the gas curtain. (right) The view of the flowing gas curtain along the stream-wise (x) direction. By changing the nozzle design the initial conditions can be changed accordingly.

nozzle whose primary amplitude (δ_0) and wavelength (λ_0) of perturbation are specified by the nozzle shape (see Figure 2). The heavy SF_6 gas inside the test section is surrounded on both sides by air, thus creating a light-heavy-light interface. The diffusive and convective processes together act to create a layer containing initial perturbations on both interfaces. Different nozzle configurations can be used to change the nature of the initial conditions. The pre-shock Atwood number defined as $A = \frac{(\rho_2 - \rho_1)}{(\rho_2 + \rho_1)}$ is $A = 0.57$, at a plane $z = 20$ mm below the nozzle. Here, ρ_2 is the density of SF_6 and acetone mixture and ρ_1 is the density of air. The Atwood number value reported here is lower than that for a pure SF_6 , air interface, due to the consideration of acetone that is used as a tracer for PLIF diagnostic. In order to maintain a stable and steady flow, the heavy gas exits through a rectangular plenum attached to the bottom wall of the test section that is maintained at a small negative pressure just sufficient to remove all of the flowing gas. The stable initial conditions are impinged upon by a $M = 1.21$ shock wave to trigger the R-M instability and study the subsequent growth. The ambient conditions of the laboratory are pressure, $P_{\text{atm}} = 0.79$ bar, temperature, $T = 25^\circ\text{C}$, speed of sound in air, $a = 346.65 \text{ m}\cdot\text{s}^{-1}$, and the advection velocity of the interface after shock, $\Delta U = 101.7 \text{ m}\cdot\text{s}^{-1}$. The following convention is used to define the direction of flow: x is the streamwise or shock direction, y is the spanwise or shock normal direction, and z is the vertical direction.

2.2. Experimental diagnostics

Measurements of the initial conditions and the dynamic flow are performed using planar laser induced fluorescence (PLIF) and particle image velocimetry (PIV) diagnostics that yield simultaneous 2D velocity-density field measurements in the x - y plane. Two dual-head, frequency-quadrupled, and frequency-doubled Nd:YAG lasers operating at wavelengths of 266 nm and 532 nm are used for PLIF and PIV measurements, respectively. Both laser beams are shaped into a thin light sheet of thickness ≤ 1.2 mm. The density and velocity measurements were performed at a plane $z = 20$ mm below the nozzle exit. The SF_6 gas is uniformly mixed with acetone vapor for PLIF measurements. The acetone vapor is generated by bubbling SF_6 through liquid acetone kept in a temperature controlled bath set at 20°C . The light from the PLIF laser is used to induce fluorescence of the acetone

present in the SF_6 . The evolving flow field after shock is captured using high sensitivity charged coupled device (CCD) cameras. The PLIF resolution is $50.5 \mu\text{m}/\text{pixel}$. The intensity calibration of the PLIF images, required for quantitative density fields, is performed using a calibration test cell. The calibration process is done before and after the experiments to accurately calculate the concentration of SF_6 . This concentration value is used as a baseline for calculating concentration at different times assuming conservation of mass within the measurement plane.

For PIV, the flow is uniformly seeded with $0.5 \mu\text{m}$ mean diameter glycol particles (mixed with SF_6 using a fog machine placed in the settling chamber) and the light scattered off these particles is imaged by a Kodak Megaplug-ES camera. The PLIF signal due to the fluorescence is removed by a Raman notch filter attached to the front of the lens. To obtain the velocity field two PIV images are separated by a time interval of $\Delta t = 2 \mu\text{s}$. The PIV vectors are then obtained by cross correlating the raw images using the commercial software INSIGHT 3G. A correlation window size of 32×32 pixels is used with suitable offsets for interrogations. A 50% overlap of the windows and a Gaussian smoothing over a 3×3 neighborhood of the interrogated field are employed to increase the spatial resolution of the measurement, and to reduce the amount of bad vectors. The PIV spatial resolution is $16.0 \mu\text{m}/\text{pixel}$, and the vector to vector spacing is $256 \mu\text{m}$.

2.3. Initial condition configurations

In order to understand the dependence of amplitude and wavelength of initial conditions on the R-M instability evolution and mixing, a dimensionless parameter representing the initial interfacial morphology can be defined [see 52,60] as follows:

$$\kappa_0 \delta_0 = \left(\sqrt{\frac{\nabla \rho' \nabla \rho'}{\rho' \rho'}} \right) \delta_0. \quad (3)$$

In Equation (3), δ_0 and κ_0 are the initial amplitude and wave number of perturbations, and ρ' is the density fluctuations across the interface. This metric has been used previously in R-M flows to scale the time [35,58], and has also been used to study initial condition dependence on mixing [44]. Mathematically, κ_0 is also referred to as the zero-crossing wavenumber that is an indicator of the spectral frequency modes present within the interface [60].

In variable density flows, κ_0 is usually computed by counting the number of times the interface crosses the zero value, N_c , which is also equivalent to sign changes of mass density fluctuation along the spanwise (y) direction. The initial wavelength of the interface is related to the number of zero crossings, N_c , as $\lambda_0 = \frac{L_y}{N_c/2} = \frac{2L_y}{N_c}$, where L_y is the total domain length in the spanwise direction. We also know that the initial wavenumber of the interface is given by $\kappa_0 = \frac{2\pi}{\lambda_0}$, so

$$\kappa_0 = \frac{\pi N_c}{L_y}. \quad (4)$$

The value of κ_0 is experimentally measured by counting N_c over a spanwise length, L_y at a line going through the center of mass of the fluid interface. Physically the parameter, $\kappa_0 \delta_0$, can also be construed as a measure of the rms slope of an interface; thus a higher value represents a more complex and corrugated initial interface. This is an important parameter

Table 1. Experimental initial condition parameters.

Initial condition	δ_0 (mm)	λ_0 (mm)	κ_0 (mm ⁻¹)	$\kappa_0 \delta_0$
Short λ mode (IC 1)	3	3.6	1.744	5.23
Long λ mode (IC 2)	3	7.2	0.872	2.62
Multi-mode ^a (IC 3)	4.6 (P), 3 (S)	16.8 (P), 3.6 (S)	0.373 (P), 1.744 (S)	4.1

^a For multi-mode initial conditions P indicates primary mode and S secondary mode.

in R-M flows because it is directly related to the amount of vorticity generated on the interface by the passage of the shock wave [52,60].

The experimental initial condition parameters are shown in Table 1. Of these three configurations, IC 1 and IC 2 are single mode initial conditions having the same initial amplitude (δ_0) but different initial wavelength (λ_0), and IC 3 is a multi-mode initial condition having two distinct modes. A mathematical representation of the single mode initial conditions can be given using the formula given in [14]. This formula was chosen owing to its simplicity and ease of use for analytical modeling of initial conditions. Based on this, the concentration profile for IC 1 can be written as follows:

$$I_1 = \frac{A_1(1 + B_1 \cos \kappa_1 y)}{1 + B_1} \exp^{-x^2 \alpha_1^2 / (1 + \beta_1 \cos \kappa_1 y)^2}, \quad (5)$$

where $A_1 = 0.63$ is the concentration intensity, $\kappa_1 = 1744 \text{ m}^{-1}$ is the wavenumber, $B_1 = 0.2$, $\alpha_1 = 836$, $\beta_1 = -0.04$ are empirical initial condition parameters, and x and y are the streamwise and spanwise direction, respectively. Similarly, IC 2 can be written as

$$I_2 = \frac{A_2(1 + B_2 \cos \kappa_2 y)}{1 + B_2} \exp^{-x^2 \alpha_2^2 / (1 + \beta_2 \cos \kappa_2 y)^2}, \quad (6)$$

where $A_2 = 0.52$, is the concentration intensity, $\kappa_2 = 872 \text{ m}^{-1}$ is the wavenumber, $B_2 = 0.7$, $\alpha_2 = 836$, $\beta_2 = -0.04$ are empirical initial condition parameters. For the multi-mode initial conditions, the following modified expression was derived empirically:

$$I_3 = 1 - \left[\cos \left(\frac{A_3(1 + B_{P3} \cos(\kappa_{P3} y_P - 735.0))}{1 + B_{P3}} \exp^{-x_P^2 \alpha_{P3}^2 / (1 + \beta_{P3} \cos(\kappa_{P3} y_P - 735.0))^2} \right) \right. \\ \left. + \cos \left(\frac{A_3(1 + B_{S3} \cos(\kappa_{S3} y_S - 129.7))}{1 + B_{S3}} \exp^{-x_S^2 \alpha_{S3}^2 / (1 + \beta_{S3} \cos(\kappa_{S3} y_S - 129.7))^2} \right) \right. \\ \left. + \cos \left(\frac{A_3(1 + B_{S3} \cos(\kappa_{S3} y_S + 400.13))}{1 + B_{S3}} \exp^{-x_S^2 \alpha_{S3}^2 / (1 + \beta_{S3} \cos(\kappa_{S3} y_S + 400.13))^2} \right) \right],$$

where $A_3 = 1$ is an empirical parameter, $\kappa_{P3} = 373.8 \text{ m}^{-1}$ is the primary wavenumber, $B_{P3} = 2.0$, $\alpha_{P3} = 512$, $\beta_{P3} = -0.04$ are empirical parameters for the primary mode, and $\kappa_{S3} = 1744 \text{ m}^{-1}$ is the secondary wavenumber, $B_{S3} = 2.2$, $\alpha_{S3} = 836$, $\beta_{S3} = -0.04$ are empirical parameters for the secondary mode.

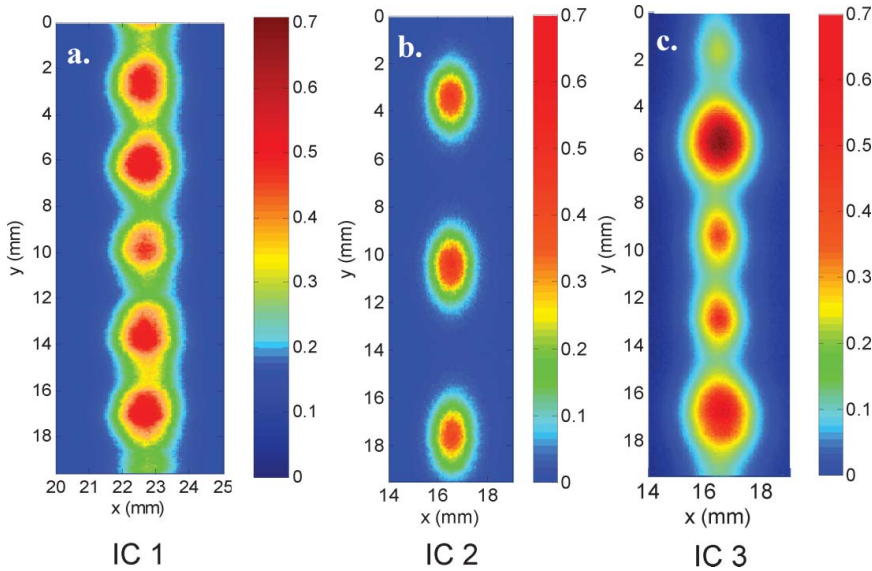


Figure 3. Initial condition concentration contour plots: (a) single mode short wavelength initial condition (IC 1), (b) single mode long wavelength initial condition (IC 2), and (c) multi-mode initial condition (IC 3). The intensity bar shows the volume fraction of SF_6 .

A contour plot of the three different experimental initial conditions taken at a plane $z = 20$ mm below the nozzle exit is shown in Figure 3. These images were obtained after correcting for laser intensity variations in the spanwise (y) direction and subtracting the background noise present in the experiments. The peak concentration (in terms of volume fraction) of SF_6 at the measurement location is $\approx 60\% \pm 5\%$ along with $\approx 20\% \pm 5\%$ of acetone and $\approx 20\% \pm 5\%$ of air. The vertical velocity of the falling gas curtain was measured using PIV (for these measurements the PIV laser sheet was reoriented vertically). The maximum value of vertical velocity of the flow is $U_z \approx 1.0 \text{ m.s}^{-1}$ at the measurement plane [44]. Very little variation in the maximum value of vertical velocity was found between the top and bottom of the falling gas curtain. The profile of $U_z(x)$ changed from Gaussian at $z = 0$ mm to a flatter profile at $z = 65$ mm.

The power spectral density (PSD) of the concentration field from a single initial condition realization at $t = 0 \text{ } \mu\text{s}$ for the three different initial condition in Table 1 are shown in Figure 4. The power spectrum was taken along a line in the spanwise (y) direction at a streamwise location (x) corresponding to the center of mass of the curtain. The PSD from multiple experiments were compared and the spectra are reproducible over many length scales. For clarity, the PSD plot shown in Figure 4 is from a single realization. The primary wavelength, λ_0 for each of the three cases is clearly seen, with small-scale noise accompanying the dominant mode(s). The small-scale fluctuations in the form of random noise present in the laboratory experiments are captured using the power spectra and are a good reference for the amount and magnitude of noise (both long wavelength and short wavelength noise) needed for accurate computational modeling of the initial conditions. This noise is mostly attributed to the random fluctuations present in our experiments, making the initial conditions slightly asymmetric, and it should be modeled for accurate comparisons with experimental results. Beyond $\kappa = 50 \text{ mm}^{-1}$, we are unable to distinguish real initial conditions fluctuations from experimental noise.

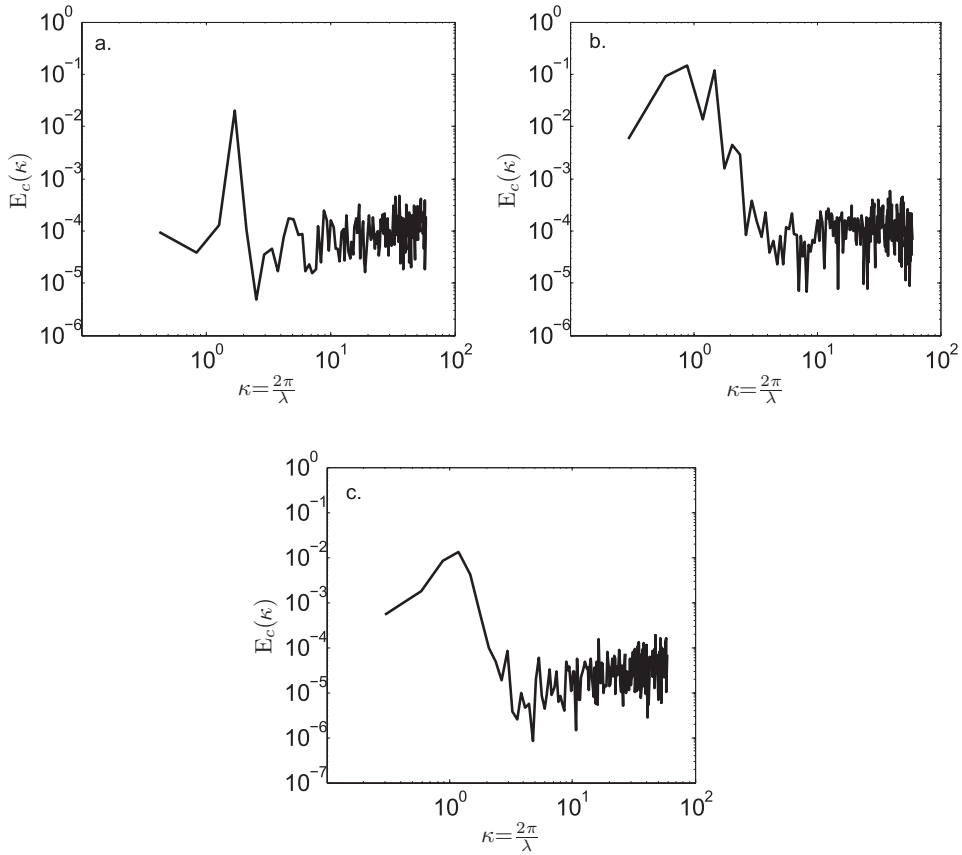


Figure 4. Power spectra of the concentration fields for three different initial condition configurations: (a) single mode short wavelength (IC 1), (b) single mode long wavelength (IC 2), and (c) multi-mode (IC 3). The dominant wavelength is evidenced by the spectral peak.

3. Results and discussion

For three different initial condition configurations, we present the bulk quantities of the flow (i.e., amplitude of the evolving interface) and smaller scale flow features (i.e., velocity and density fluctuations, turbulent kinetic energy, and Reynolds number) to better understand the mixing evolution.

3.1. Evolution and growth of R-M instability

For the three different initial conditions in Table 1, Figure 5 shows the time evolution of the density field from $t = 0 \mu\text{s}$ (shock impact time). The concentration of heavy gas (SF_6) is shown on a gray scale, with black regions indicating pure light gas (air). These images are not calibrated, hence the brightness is not indicative of the amount of mixing. The last time shown for each initial condition in Figure 5 is the last accessible time in our fixed-length test section. A visual inspection of the evolving density fields reveals differences in the mixing that are associated with the different initial conditions. For the single-mode short wavelength initial conditions (IC 1), the vortex concentration is high and the value of the

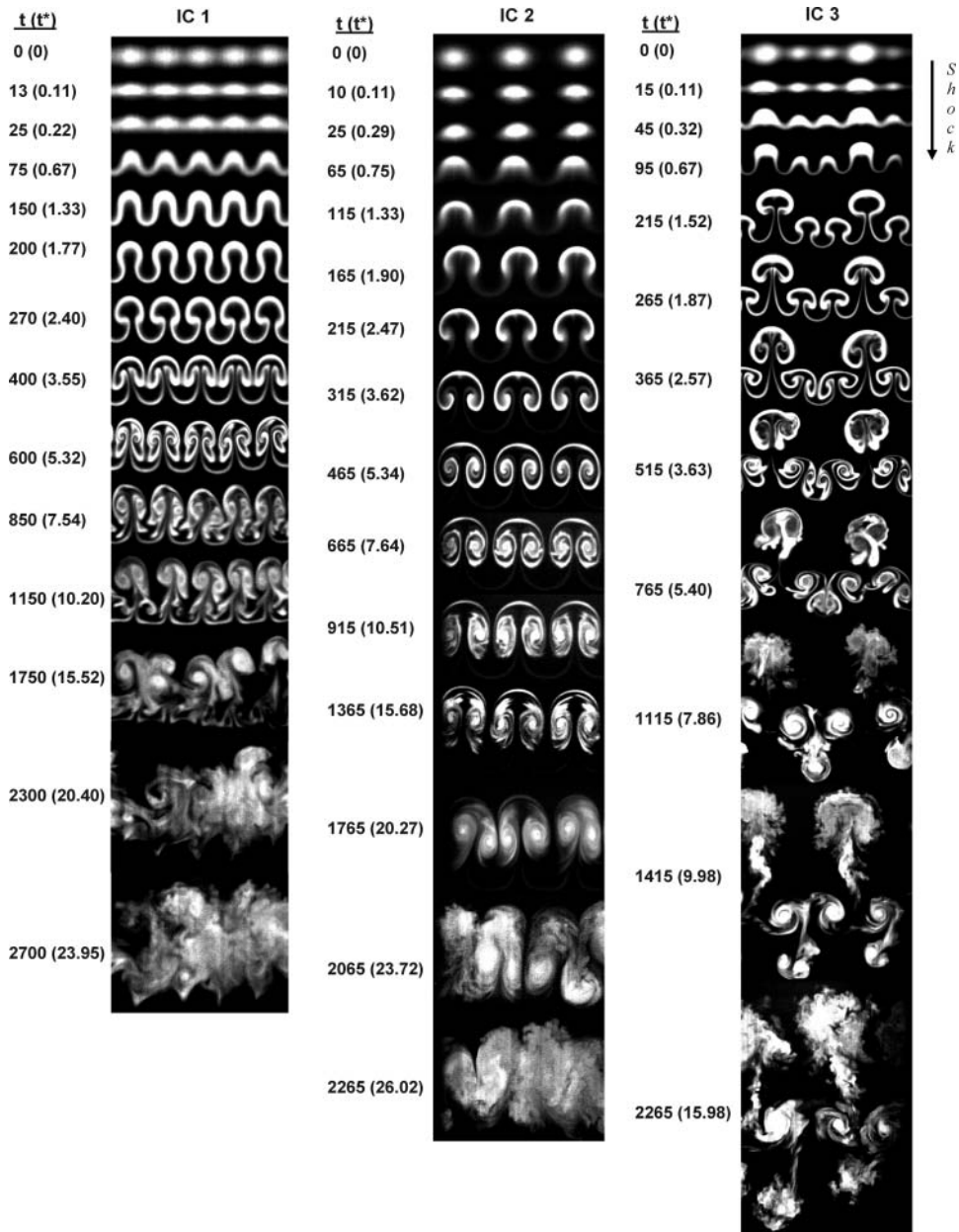


Figure 5. Time evolution of density fields for three different initial conditions. Far left: single mode short wavelength initial condition (IC 1); center: single mode long wavelength initial condition (IC 2); and far right: multi-mode initial condition (IC 3). White indicates SF_6 , and black indicates air. The time $t = 0 \mu s$ corresponds to the initial condition. In all the sets of images, t is the absolute time, and $t^* = t_{\delta_0}^*$ is the normalized time based on the initial linear growth.

dimensionless parameter $\kappa_0 \delta_0$ is the highest (see Table 1). The interface initially grows independently until the modes start to interact at about $t \approx 1100 \mu s$, as seen in Figure 5, thus leading to a more mixed state. For the single-mode long wavelength initial conditions (IC 2), the vortex concentration is less than IC 2 and the value of $\kappa_0 \delta_0$ is the lowest, so the

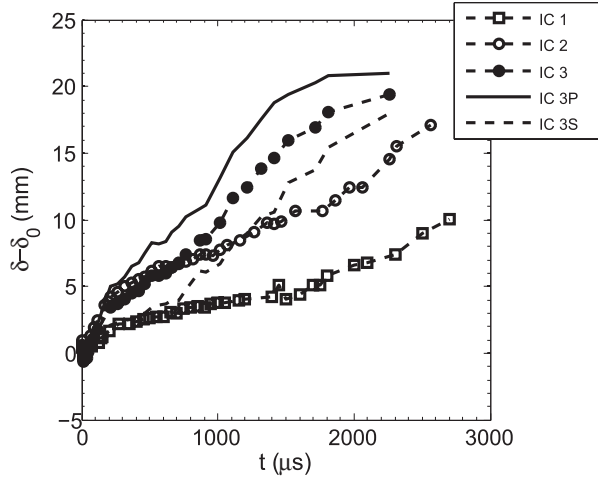


Figure 6. Amplitude of the mixing layer ($\delta - \delta_0$) with time (t). Initially, for a very short time, the amplitude appears to increase linearly with time. At late times, due to mode coupling and competition, the growth is nonlinear. In all the following figures, IC 1 denotes short wavelength initial condition, IC 2 denotes long wavelength initial condition, and IC 3 denotes multi-mode initial condition. The primary and secondary modes for the multi-mode initial condition are denoted by IC 3P and IC 3S, respectively.

modes grow independently of each other for a much longer time ($t > 1365 \mu\text{s}$). At later times, there is modal competition, as some of these modes start to outgrow others due to vortex induction, where the smaller modes are engulfed, leading to a more mixed state. Similar mixing mechanisms have also been observed for R-T instability [56]. For the case of multi-mode initial conditions (IC 3), we have a combination of a low-wavenumber large-amplitude (primary dominant) mode, and a high-wavenumber, small-amplitude (secondary) mode. The interaction between these two modes forces the secondary mode to merge quickly when compared to the IC 1 case. In contrast, the dominant mode grows independently (both in x and y dimensions), thus retaining the shape (and memory) of initial conditions until the latest observed time. In all three experiments, the flow evolves from primarily large-scale features to the much smaller scales associated with turbulence and mixing transition.

The evolution of the amplitude of the mixing layer (δ) with time is a widely used metric for R-M instability growth [e.g., 17,18,36]. We define the amplitude of the mixing layer as the total width of the interface corresponding to the difference between the upstream and downstream edges of the curtain where the SF_6 volume fraction reaches $\approx 5\%$ of its maximum value. The δ is measured over three perturbation wavelength from the center of the image, at the same span-wise location for each time. It is a measure of the nonlinear growth of the largest scales of mixing present in the flow and also reveals some differences in the nature of the mixing. Figure 6 shows a plot of $(\delta - \delta_0)$ with time for the three different initial condition configurations. For consistency, the initial amplitude of the mixing layer (δ_0) at time $t = 0$ is subtracted from the actual amplitude of the interface, δ , for each initial condition. For the multi-mode case (IC 3), the rms value of initial amplitude was used. Based on width measurements from several realizations, and after accounting for potential shot-to-shot variations in the illumination intensity (which directly affects the width for a given fixed threshold of pixel intensity), it is estimated that the widths in the present measurements are accurate to within $\pm 5\%$. For a very short period the amplitude appears

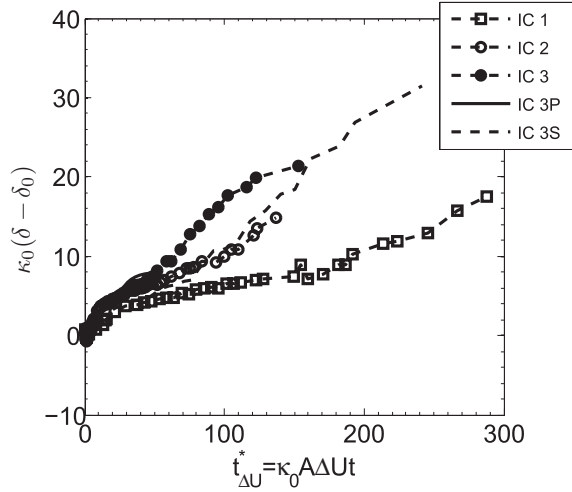


Figure 7. Normalized amplitude versus time normalized based on the advection velocity of the fluid layer does not show self-similarity for the three initial condition configurations, thus rendering this scaling not useful for initial condition studies.

to grow linearly with time (until $t \approx 95 \mu\text{s}$). Later, the nonlinear effects emerge resulting in an exponential growth of the mixing layer that reaches a plateau. For the two single-mode cases, at time $t \approx 1100 \mu\text{s}$, a secondary jump in the mixing layer amplitude is seen that may be attributed to the nonlinear mode coupling and modal competition that play an important role in increasing the amplitude growth. Figure 6 also shows that the growth rate of $(\delta - \delta_0)$ for the single-mode long wavelength case (IC 2) is higher than the single-mode short wavelength case (IC 1). This observation is consistent those reported in the study by [52] and could be attributed to the fact that $\kappa_0 \delta_0 \gg 1$. For multi-mode initial conditions, the growth rate of δ is higher than the two single-mode cases because the primary and secondary modes start to interact at a much earlier time.

To parameterize the growth of the mixing layer, the amplitude $(\delta - \delta_0)$ was non-dimensionalized with the initial wavenumber for each case, $\delta^* = \kappa_0(\delta - \delta_0)$. The time, t , was non-dimensionalized in two different ways. The first one is based on the advection velocity (ΔU) of the flow, from Equation (1), resulting in $t_{\Delta U}^* = \kappa_0 A \Delta U t$. The second scaling is based on the initial linear growth rate (δ_0), and was first proposed by [58]. The value of δ_0 is obtained by determining the slope of the best fit line that passes through the linear portions of growth curves shown in Figure 6, and the resultant scaling is $t_{\delta_0}^* = \kappa_0 A \delta_0 t$. The non-dimensional amplitude of the mixing layer (δ^*) is plotted against these two non-dimensional times, $t_{\Delta U}^*$ and $t_{\delta_0}^*$, as shown in Figures 7 and 8. With the $t_{\Delta U}^*$ scaling of Figure 7, we are unable to collapse the growth of the mixing layer. On the other hand, Figure 8 shows a self-similar growth for the two single-mode initial conditions (IC 1 and IC 2) until non-dimensional time $t_{\delta_0}^* \approx 12$, with the $t_{\delta_0}^*$ scaling. This indicates that this time normalization might be useful for single mode initial conditions. The multi-mode initial conditions have a higher growth rate, confirming our visual observations of Figure 5 that modal interactions occur faster in the multi-modal configuration. The growth of the amplitude of the mixing layer for the two single mode experiments can be modeled as $\sim t^{0.67}$ (shown by semi-dotted line in Figure 8). This confirms the modeling used previously by [18] and others. From these experiments, we determine that while the single-mode initial

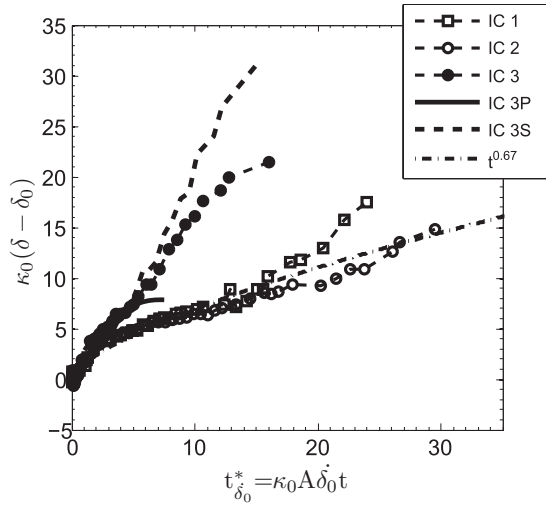


Figure 8. Normalized amplitude versus time normalized with the initial linear growth rate value, first proposed and used by [58]. Such a non-dimensionalization works for the single mode initial conditions, but not for the multi-mode case (IC 3). The $t^{0.67}$ used by [18] is a good fit for the amplitude growth rate for the single mode initial conditions.

conditions follow growth rates similar to those proposed earlier, the multi-mode initial conditions grow at a much faster rate. Growth rate models must account for differences in initial conditions if they are to capture the bulk of the fluid mixing. These models do not capture molecular mixing differences, because those occur at scales smaller than the amplitude of the mixing layer.

3.2. Turbulence statistics

If we are to understand mixing differences from different initial conditions, we must look at all of the energy-containing scales in the flow. Turbulence modeling has long assumed a self-similarity of turbulence quantities to simplify the mathematics of the modeling. Kolmogorov [61] argued that not only does the directional information gets lost as the energy passes down the cascade, but that all information about the geometry of the eddies also gets lost. As a result of these assumptions, the statistics of the small-scale motions are universal in the sense that they are similar in every high Reynolds number turbulent flow, independent of the mean flow field and the boundary conditions. Turbulence and mixing induced by shock-driven hydrodynamic instabilities have a few distinct features in comparison to classical turbulent flows. Anisotropy and inhomogeneities arise due to various factors ranging from initial condition variations, the presence of shocks, material discontinuities, and associated baroclinic effects. Detailed turbulence measurements are needed to clearly understand these differences in order to better model such flows. From an experimental point of view, this requires collecting data on the time evolution of velocity and density statistics and calculating various turbulence quantities from them. In this section, we will present some of the important experimentally measurable quantities that impact mixing in variable density fluid flows. The turbulence quantities presented below were calculated from an instantaneous realization and not ensemble averaged, as would normally be done

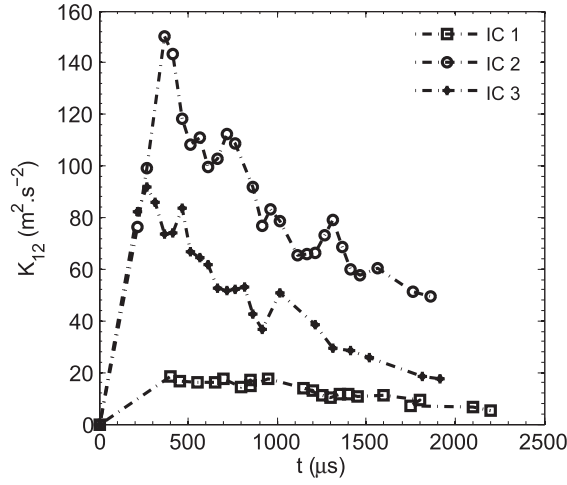


Figure 9. Turbulent kinetic energy based on 2D measurements showing the dissipation of energy from large scales to smaller scale mixing.

in experimental measurements. This averaging is consistent with statistics calculated from large eddy simulations, and we are unable to perform the approximately one thousand experiments needed to have converged, ensemble-averaged statistics.

3.2.1. Turbulent kinetic energy

The 2D turbulent kinetic energy K is defined as the root mean square (rms) of the velocity fluctuations in two dimensions:

$$K_{12} = \frac{1}{2} \left(\overline{u_1'^2} + \overline{u_2'^2} \right), \quad (7)$$

where u_1' is the velocity fluctuations in the direction of the shock wave or streamwise direction (x) and u_2' is the velocity fluctuations in the shock normal or spanwise direction (y). Before calculating the turbulent kinetic energy, velocity fluctuations present in the flow with the 2D (x - y plane) PIV data at a fixed time are measured as follows:

$$u_i'(x, y) = u_i(x, y) - \overline{u_i(x)}, \quad (8)$$

$$\overline{u_i'^2} = \overline{u_i'(x, y)^2}, \quad (9)$$

where $i = 1, 2$ represents components in the x , and y directions, respectively. It should be noted that $\overline{u_i(x)}^y = \overline{u_i(x, y)}^y(x)$. From the experimental velocity field data, the 2D turbulent kinetic energy (K_{12}) was calculated for the three initial condition configurations over time and is shown in Figure 9. For all three cases, the turbulent kinetic energy increases initially (due to the baroclinic vorticity depositing energy into the flow) and starts to decrease indicating the energy dissipation process and transfer of energy from large scales to smaller scales. Our experimental measurements are consistent to within 5% of the turbulent kinetic energy results of [62] where they numerically simulated the gas curtain problem. The small

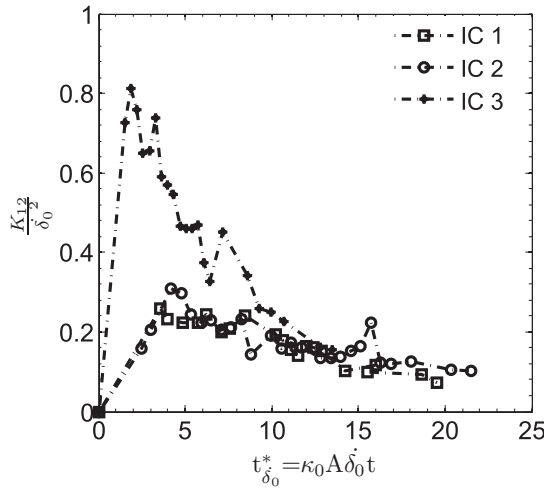


Figure 10. The normalized 2D Turbulent kinetic energy plotted against normalized time reaches an asymptotic value of turbulent kinetic energy after $t_{\delta_0}^* \approx 12$.

difference could be attributed to the fact that the numerical simulations include 3D effects. At late times, the differences in the 2D and 3D turbulent kinetic energy values in experiments and simulation is $\approx 10\text{--}15\%$, owing to the effect of the third velocity component. Also, in a recent work by [63], it was reported that seeding the heavy gas only versus seeding the whole flow does not have a large impact on turbulent kinetic energy results when it is calculated as shown in Equation (7); hence, our measurements are independent of the particle seeding method.

In order to test initial condition dependence, the 2D turbulent kinetic energy was normalized by dividing K_{12} by square of the initial linear growth rate (δ_0) for the three different experimental runs. In general, one can use the mean convection velocity of the flow, ΔU , to normalize the turbulent kinetic energy, K_{12} , but ΔU is the same for each experiment and does not account for the initial conditions of the interfaces. From Figure 8, the normalization based on δ_0 shows self-similarity for different single-mode initial condition configurations, so we scale K_{12} with δ_0 . The normalized turbulent kinetic energy is plotted against normalized time in Figure 10. The important observation from this figure is that the turbulent kinetic energy for all three cases reaches an asymptotic value after $t_{\delta_0}^* \approx 12$, indicating self-similar value of K at late times for different initial condition configurations. Although K_{12} decays to an asymptotic value for all three experiments, we see differences in the large-scale mixing after $t^* = 12$ for all the three cases in Figure 5. This suggests that homogeneity is obtained at small scales, but the large scale turbulence may still be asymmetric and anisotropic. Also, the density fields in Figure 5 indicate late-time memory of the initial conditions. This was also confirmed from the late-time density power spectra shown in Figure 11. When comparing the late time spectra with the initial condition spectra for the three different initial conditions (Figure 4), we still see an imprint of the primary wavenumber mode, indicating persistence of the initial condition modes into late times when there is significant small-scale mixing. Figure 11 shows that the inertial ranges for the spectra have increased, indicating an energy cascade and transition to a more mixed and turbulent state.

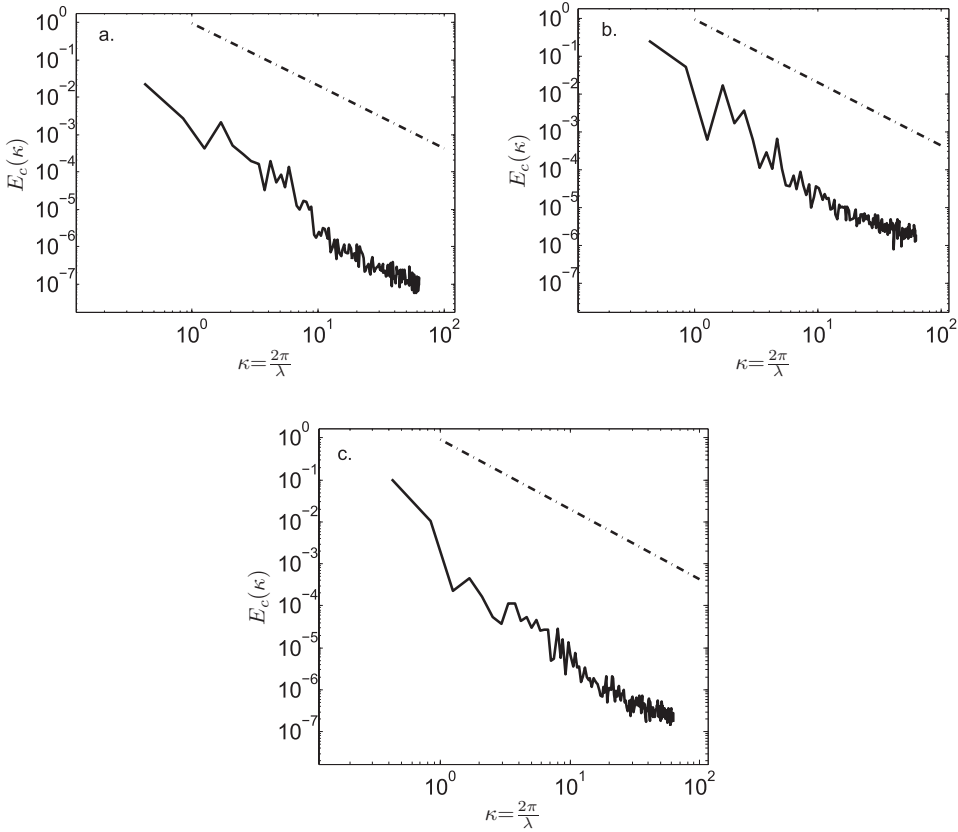


Figure 11. The late-time power spectra of the concentration fields at $t \approx 2000 \mu\text{s}$ for three different initial condition configuration: (a) single mode short wavelength initial conditions (IC 1), (b) single mode long wavelength initial condition (IC 2), and (c) multi-mode initial conditions (IC 3). The dominant wavelength is preserved in each case at late times indicating initial condition dependence on R-M mixing. The dotted line represents $\kappa^{-5/3}$ slope, for reference.

3.2.2. Turbulent Reynolds number

In turbulence, the range of flow scales increases continuously as the energy spectrum broadens. Different Reynolds numbers can be defined to measure large scale and small scale flow features. The most commonly used is the bulk Reynolds number, defined as $Re_\delta = \frac{\delta \dot{\delta}}{\nu}$ (where δ is the rate of growth of the mixing layer and ν is the kinematic viscosity of the fluid), that is a measure of the large scales [46]. Although δ and $\dot{\delta}$ are relatively easy to measure in experiments, the Re_δ does not accurately capture the inertial and viscous force differences that govern mixing in R-M flows. We propose using Reynolds numbers that are more relevant to understanding turbulent mixing. The turbulent Reynolds number based on 2D turbulent kinetic energy defined as $Re_K = \frac{\sqrt{K_{12}} \delta}{\nu}$ represents the magnitude of turbulent transport versus viscous transport. It is important in measuring the small-scale flow features and understanding energy contained in the smaller scales. In turbulent flows, the Taylor microscale is the largest length scale at which fluid viscosity significantly affects the dynamics of turbulent eddies in the flow [64]. Thus, a Taylor microscale Reynolds number is often used and can be defined using the isotropic formula $Re_\lambda = \sqrt{\frac{20}{3}} Re_K$.

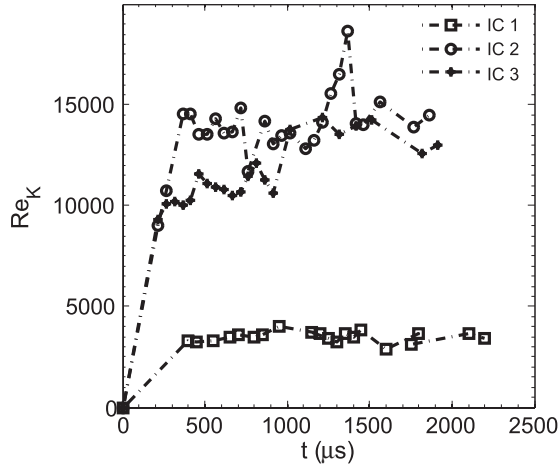


Figure 12. Turbulent Reynolds number for three different initial conditions.

Here, we will present measurements of turbulent Reynolds number (Re_K) and Taylor Reynolds number (Re_λ). The plot of evolution of Re_K for different initial conditions is shown in Figure 12. The turbulent Reynolds number increases with time indicating that the fluid mixing layer is turbulent. The evolution of self-similar turbulent Reynolds number denoted as $Re_K(\delta_0/\lambda_0)^{-1.5}$ plotted against $t_{\delta_0}^*$ is shown in Figure 13. From the gradient diffusion hypothesis [see 46], for asymptotic self-similarity it is necessary that Re_K grows as a function of the mixing layer width, δ_0/λ_0 , and reaches a steady asymptotic state, which is not seen from Figure 13. This points to the fact that there is a mismatch between the lower-order terms in the self-similar formulae for the kinetic energy and viscous dissipation. Thus even though the amplitude of the mixing layer and the turbulent kinetic energy show asymptotic self-similarity, the approach to a complete self-similarity occurs much later than we observe in our experiments. The Taylor microscale Reynolds number also steadily increases starting from zero and reaching a maximum value of $Re_\lambda = 165$ for IC 1,

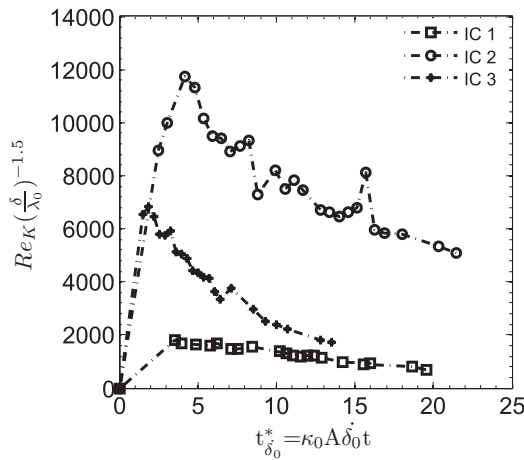


Figure 13. Time variation of self-similar Reynolds number.

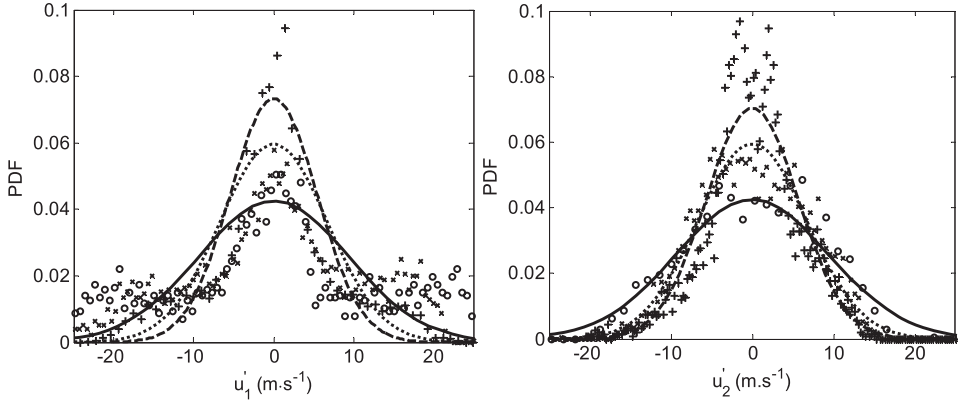


Figure 14. Probability density functions of velocity fluctuations for single mode long wavelength IC 2 configuration. $t(t_{00}^*) = 315 \mu\text{s}$ (3.62) (\circ : experimental pdf, solid line: least square Gaussian fit). $t(t_{00}^*) = 965 \mu\text{s}$ (11.08) (\times : experimental pdf, dotted line: least square Gaussian fit). $t(t_{00}^*) = 1865 \mu\text{s}$ (21.42) ($+$: experimental pdf, dash line: least square Gaussian fit given by Equation (10)).

$Re_\lambda = 316$ for IC 2, and $Re_\lambda = 290$ for IC 3, indicating moderate to high turbulence inside the mixing layer.

3.2.3. Probability density function and rms of velocity fluctuations

Turbulence is characterized by the intermittent generation of very large gradients and velocity differences, and the probability density functions of these parameters gives us an indication of the intermittency present in the flow. Intermittency has several meanings, but the most apt from a turbulence perspective is the tendency of the probability distributions of turbulent quantities to develop long tails along with non-Gaussian distributions [65]. It has also been observed that the extreme tails become stronger as the Reynolds number increases.

The probability density functions (pdf's) for our experiments were calculated by plotting the area histograms of the turbulence quantities. A least-squares Gaussian distribution, given as

$$P(x) = \frac{1}{\sqrt{(2\pi)\sigma}} \exp\left(-\frac{(x - \mu)^2}{2\sigma^2}\right) \quad (10)$$

was used to measure the deviation of the experimental pdf from a Gaussian distribution. The pdf's of velocity fluctuations, u'_1 and u'_2 , for the two initial condition configurations (IC 2 and IC 3) at early and late times are shown in Figures 14 and 15. The pdf's show that the tail of the distribution becomes narrower with increasing time, corresponding to increasing turbulent Reynolds number (Re_K) showing that the intermittency in the flow is reducing and the turbulence is decaying. The fit given by Equation (10) also shows that the distribution becomes more Gaussian with increasing time.

The rms of velocity fluctuations, related to the variance, is given as

$$\sigma_{u_i}(x) = \sqrt{u_i'^2(x, y)^y}, \quad (11)$$

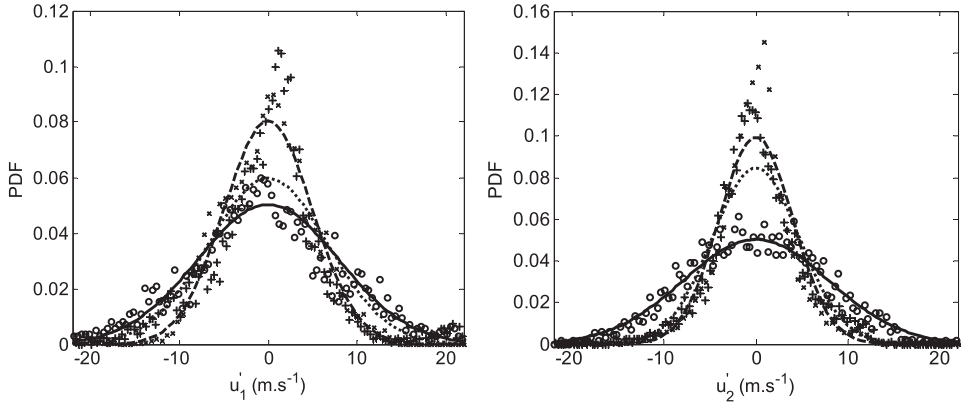


Figure 15. Probability density functions of velocity fluctuations for multi-mode IC 3 configuration. $t(t_{\delta_0}^*) = 465 \mu\text{s}$ (3.28) (\circ : experimental pdf, solid line: least square Gaussian fit). $t(t_{\delta_0}^*) = 965 \mu\text{s}$ (6.49) (\times : experimental pdf, dotted line: least square Gaussian fit). $t(t_{\delta_0}^*) = 1815 \mu\text{s}$ (12.80) ($+$: experimental pdf, dash line: least square Gaussian fit given by Equation (10)).

where $i = 1, 2$, represents the rms in streamwise (x) direction and spanwise (y) directions. The rms of the velocity fluctuations in both the directions across the fluid layer at different times is shown for two initial condition cases (IC 2 and IC 3) in Figures 16 and 17. For homogenous and isotropic turbulence, the rms of the velocity fluctuations should be the same in all the directions. From the figures, the rms of velocity fluctuations in the shock direction (u'_1) is much higher than that in the spanwise (u'_2) direction indicating more energy is initially present in the shock direction (x). Also, the shape of the two curves are different with strong aperiodicity in shock normal direction (y). With time the energy is distributed to different scales present in the flow, and the rms of u'_1 and u'_2 are approaching a homogeneous state with similar profiles and values everywhere across the fluid layer. The rms of the velocity fluctuations when measured across the mixing layer shows a strong anisotropy in the shock direction. This indicates turbulence asymmetry in the flow, and it was also observed in the studies by [37] and [44].

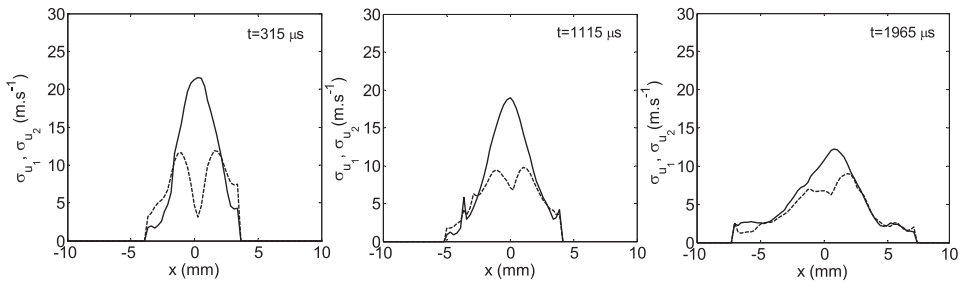


Figure 16. The rms of velocity fluctuations, in the shock direction σ_{u_1} (solid line), and shock normal direction σ_{u_2} (dashed line) for single mode long wavelength IC 2 configuration. The corresponding non-dimensional time is $t_{\delta_0}^* = 3.62$ ($t = 315 \mu\text{s}$), 12.81 ($t = 1115 \mu\text{s}$), and 22.57 ($t = 1965 \mu\text{s}$).

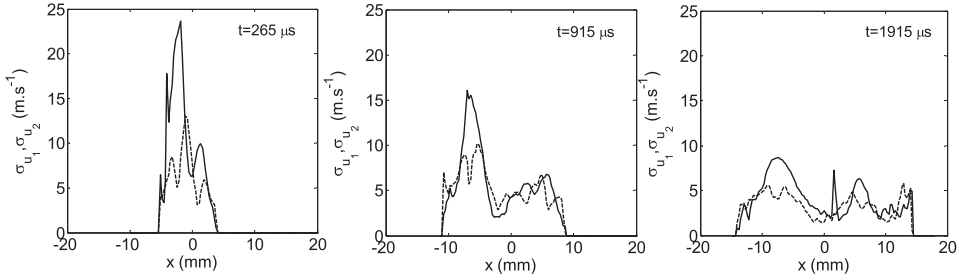


Figure 17. The rms of velocity fluctuations, in the shock direction σ_{u_1} (solid line), and shock normal direction σ_{u_2} (dashed line) for multi-mode IC 3 configuration. The corresponding non-dimensional time is $t_{\delta_0}^* = 1.87$ ($t = 265 \mu s$), 6.45 ($t = 915 \mu s$), and 13.51 ($t = 1915 \mu s$).

3.2.4. Density of the mixing layer

Recent numerical results for variable density flows have shown that, at very low Atwood numbers, a fluid mixing layer remains symmetric around the center of mass. As the Atwood number is increased, the flow becomes more asymmetric and non-Boussinesq [46]. The present high Atwood number R-M experiments can provide a test for this behavior through use of the density maps obtained from the quantitative PLIF measurements.

The mean density (averaged in the spanwise, y , direction) for the case of the single-mode long wavelength initial condition (IC 2) is shown in Figure 18. The density initially increases after shock compression and then decreases as the fluids mix together. Before the shock wave hits the curtain, the initial density profile is Gaussian. After interaction with the shock, the density profile becomes discontinuous showing multiple peaks due to distinct SF_6 and air pockets. When the fluid layer mixes, the density profile becomes more uniform across the mixing layer. With time, the mixing layer with respect to the center of

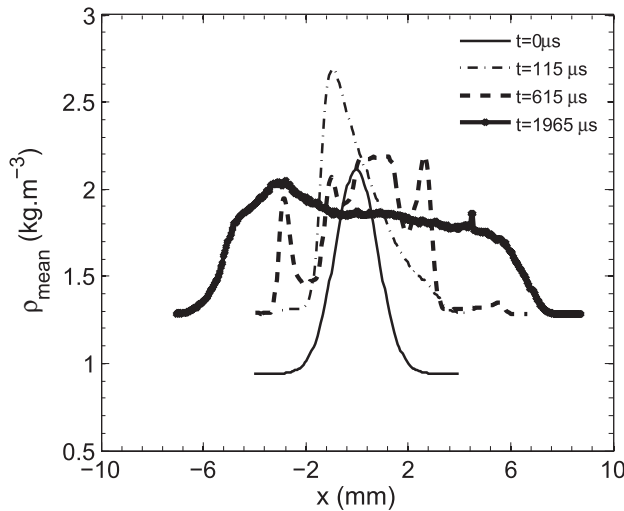


Figure 18. Density profile at different times (shown in the legend) across the mixing layer for IC 2. The asymmetric behavior of the mixing layer from the center of mass ($x = 0$) is seen from this plot. The shock wave moves from left to right.

mass starts to show asymmetric behavior that becomes pronounced at late times. Initially, at $t = 115 \mu\text{s}$, the density profile is asymmetric with more mass located in the upstream side (with respect to the motion of shock wave) of the center of mass. At late times, e.g., $t = 615 \mu\text{s}$, more mass is found on the downstream side, since the fluid is being advected in that direction. The mixing layer is asymmetric and moderately non-Boussinesq.

3.2.5. Density-specific volume correlation

In variable density flows, we use the parameter, b , the density-specific volume correlation, to characterize mixedness. During the mixing process, b plays an important role in mediating the mass transport by appearing as an unclosed term in the evolution equation for mass transport [66]. The parameter b is defined as the product of the density and volume fraction fluctuations of the fluids present in the flow and can be mathematically represented as

$$b = -\overline{\rho' \left(\frac{1}{\rho} \right)'} \quad (\text{or}) \quad b = \overline{\bar{\rho} \left(\frac{1}{\rho} \right)} - 1. \quad (12)$$

By definition, b is non-negative and equals zero when two fluids are fully mixed or for homogeneous fluids. In shock-accelerated R-M flows, initially, the density fluctuations are small, but at later times b is an important metric that can be used to quantify the amount of mixing. A high value of b indicates regions of unmixed fluid and a low value of b indicates a well mixed state. Using the 2D density field data at a given time, we calculate b in the following way:

$$\rho'(x, y) = \rho(x, y) - \overline{\rho(x)}^y, \quad (13)$$

$$\left(\frac{1}{\rho(x, y)} \right)' = \frac{1}{\rho(x, y)} - \left(\frac{1}{\rho(x)} \right)^y, \quad (14)$$

$$b(x, y) = -\rho'(x, y) \left(\frac{1}{\rho(x, y)} \right)', \quad (15)$$

$$\overline{b(x)} = \overline{-\rho'(x, y) \left(\frac{1}{\rho(x, y)} \right)'}, \quad (16)$$

$$b(x) = \overline{\rho(x)}^y \left(\frac{1}{\rho(x)} \right)^y - 1, \quad (17)$$

$$\bar{b} = \overline{b(x)}, \quad (18)$$

$$b^* = \frac{\bar{b}}{\bar{b}_0}. \quad (19)$$

In the above set of equations, $\rho(x, y)$ is the 2D density field, the inverse of density field is the corresponding volume fraction field, and $b(x, y)$ is the 2D density-specific volume correlation field. It should be noted that $\overline{\rho(x)}^y = \overline{\rho(x, y)}^y(x)$, and similar expression can be written for the volume fraction field. The terms $\rho(x)$, $\frac{1}{\rho(x)}$, $b(x)$ represent the density, volume fraction, and density-specific volume correlation across the fluid interface in the shock direction, \bar{b}_0 is the mean value of b at time $t = 0$. The evolution of the mean value

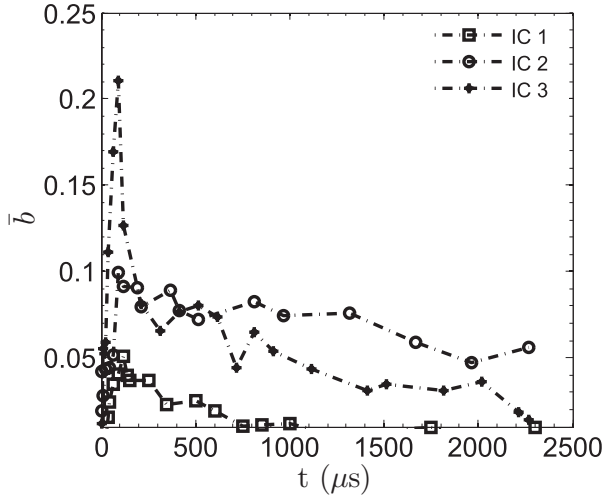


Figure 19. Evolution of mean density-specific volume correlation, \bar{b} .

of the density-specific volume correlation, \bar{b} , for the three initial condition configurations is shown in Figure 19. For all three cases, \bar{b} increases after the incident shock wave passes through the interface and then starts to decrease as the two fluids mix. The value of \bar{b} at late times is lower for the highest value of $\kappa_0 \delta_0$ (IC 1), indicating that the fluid interface is more uniformly mixed. A more complex/corrugated interface leads to a more well-mixed state, consistent with the results of [52]. The normalized value of b , denoted as b^* and defined in Equation (19), is plotted versus $t_{\delta_0}^*$ in Figure 20. For all IC cases, b^* reaches the same asymptotic value of $b^* \approx 3$, after $t_{\delta_0}^* \geq 12$. This asymptotic behavior is consistent with the observed behavior of the 2D turbulent kinetic energy (Figure 10).

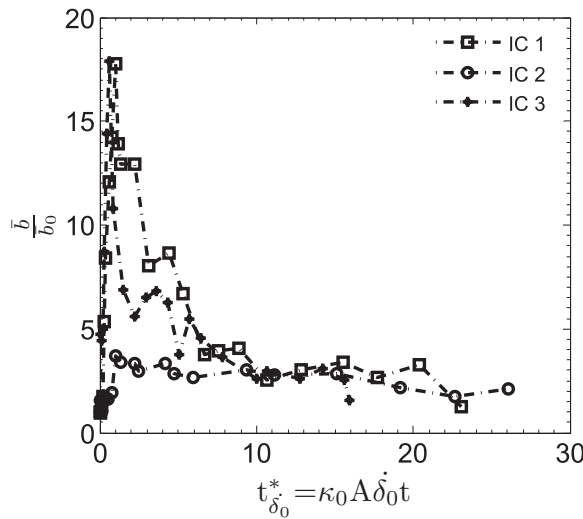


Figure 20. Plot of normalized density-specific volume correlation versus normalized time reveals asymptotic behavior of b after $t_{\delta_0}^* \approx 12$.

The late-time power spectra of the concentration fields indicate a mixing transition from large scales to smaller scales. The values of 2D turbulent kinetic energy, K_{12} , and density-specific volume correlation, b , the two unclosed terms the turbulence model [66], for the three different initial condition configurations, suggest that the sub-grid scale turbulence models may be appropriately applied after this normalized time to capture mixing transitions to smaller scales. Although the small scales present in the flow reach a homogeneous state of mixing (seen from the two dimensional K_{12} and b values), the large scale turbulence is asymmetric and the large scale flow features preserve memory of the initial condition modes. The probability density function of the velocity field shows that the turbulence is decaying with time. The non-Boussinesq and asymmetric nature of turbulence is also confirmed from the density and velocity fields. These results give us an indication that shock-driven flows are time- and initial condition dependent and should be modeled differently than classical turbulence. The results from this work will be useful for development and validation of predictive turbulence closure models [67,68] for variable density flows. More work in the future is necessary to confirm the exact state of mixing and turbulence in unsteady variable density flows.

4. Conclusions

A series of experiments were conducted to test the dependence of initial amplitude (δ_0) and wavenumber (κ_0) of perturbations on turbulence and mixing in a shock-accelerated flow with an unstable Richtmyer–Meshkov (R-M) fluid layer. Single and multi-mode membrane-free initial conditions in the form of a gas curtain having a light-heavy-light configuration (air-SF₆-air) and an Atwood number of $A = 0.57$ were used in our experiments and were driven by a planar shock wave with Mach number $M = 1.21$. Various statistics were calculated from these data, and the following important conclusions are made from this study.

1. Time series of the density fields of the R-M instability (shown in Figure 5) for three different initial condition configurations show some qualitative differences in the nature of mixing. Modal merging and competition are two important phenomena aiding mixing in R-M flows. The numerical hypothesis that “memory of initial conditions can be retained in the flow” was corroborated qualitatively and also quantitatively using the power spectra of the density fields.
2. Two different types of scaling were used to non-dimensionalize the time, t ; one using the advection velocity of the flow, ΔU , and other using the linear growth rate, δ'_0 (proposed first by [58]). It was found that t scaled with δ'_0 , henceforth referred to as normalized time, $t_{\delta'_0}^*$, gives a satisfactory collapse for the single mode initial condition (IC 1 and IC 2) growth rates, but not for the multi-mode case.
3. The 2D turbulent kinetic energy, K_{12} , normalized with $\delta'_0{}^2$, versus normalized time, $t_{\delta'_0}^*$, reaches an asymptotic value after $t_{\delta'_0}^* \approx 12$ for all three initial condition cases.
4. The turbulent Reynolds number and Taylor microscale Reynolds number indicate that the fluid layer is moderately turbulent to highly turbulent for different initial condition configurations. Moreover the self-similar Reynolds number plotted vs $t_{\delta'_0}^*$ does not show a self-similar state, indicating that the fluid layer is non-homogeneous and the gradient diffusion hypothesis is not satisfied. The asymmetric behavior of the mixing layer is also seen from the rms of velocity fluctuations and density plots, suggesting turbulence asymmetry and non-Boussinesq behavior.

5. The density-specific volume correlation, b , shows more mixing for higher values of $\kappa_0 \delta_0$. Normalized b plotted versus normalized time reaches an asymptotic value after $t_{\delta_0}^* \approx 12$ for all three initial condition cases, similar to that of the turbulent kinetic energy.
6. The memory of the initial conditions is retained in the bulk of the flow. A few statistics (such as K_{12} , b , rms of velocity fluctuations), that govern the smaller scale mixing in the flow reach an asymptotic state when scaled with parameters that capture the wavelength and amplitude characteristics of the initial conditions.

These results can help to guide the timing of the initialization of turbulence models (such as BHR turbulence model, [66]) as well as initial values for transport model terms in simulations of unsteady shock-driven and variable density flows.

Acknowledgements

This research work was supported by Los Alamos Laboratory Directed Research & Development program through Directed Research (LDRD-DR) on “Turbulence by Design,” research project number 20090058DR. The authors would like to acknowledge the help rendered by a former member of our team, Dr B.J. Balakumar, with data analysis and valuable discussions. We also thank our collaborators F.F. Grinstein, A.A. Gowardhan, J.R. Ristorcelli, M.J. Andrews, R.A. Gore, and D. Livescu for useful insights and discussions toward this research.

References

- [1] R.D. Richtmyer, *Taylor instability in shock acceleration of compressible fluids*, Commun. Pure Appl. Math. 13 (1960), pp. 297–319.
- [2] E.E. Meshkov, *Instability of the interface of two gases accelerated by a shock wave*, Fluid Dyn. 4 (1969), pp. 151–157.
- [3] T. Phama and D.I. Meiron, *A numerical study of Richtmyer–Meshkov instability in continuously stratified fluids*, Phys. Fluids A 5 (1993), pp. 344–368.
- [4] K.O. Mikaelian, *Turbulent mixing generated by Rayleigh–Taylor and Richtmyer–Meshkov instabilities*, Physica D 36 (1989), pp. 343–357.
- [5] J.D. Lindl and W.C. Mead, *Two-dimensional simulation of fluid instability in laser-fusion pellets*, Phys. Rev. Lett. 34 (1975), pp. 1273–1276.
- [6] J.D. Lindl, R.L. McCrory, and E.M. Campbell, *Progress toward ignition and burn propagation in inertial confinement fusion*, Phys. Today 377 (1992), pp. 32–40.
- [7] R. Betti, C.D. Zhou, K.S. Anderson, L.J. Perkins, W. Theobald, and A.A. Soldov, *Shock ignition of thermonuclear fuel with high areal density*, Phys. Rev. Lett. 98 (2007), 155001.
- [8] Y. Aglitskiy, A.L. Velikovich, M. Karasik, N. Metzler, S.T. Zalesak, A.J. Schmitt, L. Philips, J.H. Gardner, V. Serlin, J.L. Weaver, and S.P. Obenschain, *Basic hydrodynamics of Richtmyer–Meshkov-type growth and oscillations in the inertial confinement fusion-relevant conditions*, Philos. Trans. R. Soc. London, Ser. A 368 (2010), pp. 1739–1768.
- [9] J. Kane, B.A. Remington, and R.P. Drake, *An evaluation of the Richtmyer–Meshkov instability in supernova remnant formation*, Astrophys. J. 511 (1999), pp. 335–340.
- [10] B.E. Gelfand, S.V. Khomik, A.M. Bartenev, S.P. Medvedev, H. Grönig, and H. Olivier, *Detonation and deflagration initiation at the focusing of shock waves in combustible gaseous mixture*, Shock Waves 10 (2000), pp. 197–204.
- [11] A.R. Miles, M.J. Edwards, and J.A. Greenough, *Effects of initial conditions on compressible mixing in supernova-relevant laboratory experiments*, Phys. Astron. 298 (2005), pp. 17–24.
- [12] M.B. Zellner, W.V. McNeil, J.E. Hammerberg, A.W.O. R. S. Hixson, R.T. Olson, J.R. Payton, P.A. Rigg, N. Routley, G.D. Stevens, W.D. Turley, L. Veaser, and W.T. Buttler, *Probing the underlying physics of ejecta production from shocked Sn samples.*, J. Appl. Phys. 103 (2008), 123502.
- [13] K.O. Mikaelian, *Richtmyer–Meshkov instabilities in stratified fluids*, Phys. Rev. A 31 (1985), pp. 410–419.
- [14] K.O. Mikaelian, *Numerical simulations of Richtmyer–Meshkov instabilities in finite-thickness fluid layers*, Phys. Fluids 8 (1996), pp. 1269–1292.

- [15] M. Brouillette and B. Sturtevant, *Experiments on the Richtmyer–Meshkov instability: Small-scale perturbations on a plane interface*, Phys. Fluids A 5 (1993), p. 916.
- [16] D.L. Youngs, *Numerical simulation of mixing by Rayleigh–Taylor and Richtmyer–Meshkov instabilities*, Laser Part. Beams 12 (1994), pp. 725–750.
- [17] M. Vetter and B. Sturtevant, *Experiments on the Richtmyer–Meshkov instability of an air/SF₆ interface*, Shock Waves 4 (1995), pp. 247–252.
- [18] G. Dimonte, C.E. Frerking, and M. Schneider, *Richtmyer–Meshkov instability in the turbulent regime*, Phys. Rev. Lett. 74 (1995), pp. 4855–4861.
- [19] X.L. Li and Q. Zhang, *A comparative numerical study of the Richtmyer–Meshkov instability with nonlinear analysis in two and three dimensions*, Phys. Fluids 9 (1997), pp. 3069–3077.
- [20] F. Poggi, M. Thorembey, and G. Rodriguez, *Velocity measurements in turbulent gaseous mixtures induced by Richtmyer–Meshkov instability*, Phys. Fluids 10 (1998), pp. 2698–2700.
- [21] O. Sadot, L. Erez, U. Alon, D. Oron, L. Levin, G. Erez, G. Ben-Dor, and D. Shvarts, *Study of nonlinear evolution of single-mode and two-bubble interaction under Richtmyer–Meshkov instability*, Phys. Fluids Lett. 80 (1998), pp. 1654–1657.
- [22] P.M. Rightley, P. Vorobieff, R. Martin, and R.F. Benjamin, *Experimental observations of the mixing transition in a shock-accelerated gas curtain*, Phys. Fluids 11 (1999), pp. 186–200.
- [23] M.H. Anderson, B.P. Puranik, J.G. Oakley, P.W. Brooks, and R. Bonazza, *Shock tube investigation of hydrodynamic issues related to inertial confinement fusion*, Shock Waves 10 (2000), pp. 377–387.
- [24] J.G. Wouchuk, *Growth rate of the linear Richtmyer–Meshkov instability when a shock is reflected*, Phys. Rev. E 63 (2001), 056303.
- [25] S.I. Abarzhi, *Asymptotic behavior of three-dimensional bubbles in the Richtmyer–Meshkov instability*, Phys. Fluids 13 (2001), pp. 2866–2875.
- [26] D. Oron, L. Arazi, D. Kartoon, A. Rikanati, U. Alon, and D. Shvarts, *Dimensionality dependence of the Rayleigh–Taylor and Richtmyer–Meshkov instability late-time scaling laws*, Phys. Plasmas 8 (2001), pp. 2883–2889.
- [27] M. Brouillette, *The Richtmyer–Meshkov instability*, Annu. Rev. Fluid Mech. 34 (2002), pp. 445–468.
- [28] M. Vandenboomgaerde, S. Gauthier, and C. Mugler, *Nonlinear regime of a multimode Richtmyer–Meshkov instability: A simplified perturbation theory*, Phys. Fluids 14 (2002), 1111–1111–22.
- [29] C. Matsuoka, K. Nishihara, and Y. Fukuda, *Nonlinear evolution of an interface in the Richtmyer–Meshkov instability*, Phys. Rev. E 67 (2003), 036301.
- [30] J.W. Jacobs and V.V. Krivets, *Experiments on the late-time development of single-mode Richtmyer–Meshkov instability*, Phys. Fluids 17 (2005), 034105–034105–10.
- [31] D. Hill, C. Pantano, and D. Pullin, *Large-eddy simulation and multiscale modelling of a Richtmyer–Meshkov instability with reshock*, J. Fluid Mech. 557 (2006), pp. 29–61.
- [32] C. Tomkins, S. Kumar, G. Orlicz, and K. Prestridge, *An experimental investigation of mixing mechanisms in shock-accelerated flow*, J. Fluid Mech. 611 (2008), pp. 131–150.
- [33] O. Schilling, M. Latini, and W.S. Don, *Physics of reshock and mixing in single-mode Richtmyer–Meshkov instability*, Phys. Rev. E 76 (2007), 026319.
- [34] D. Ranjan, J. Niederhaus, B. Motl, M. Anderson, J. Oakley, and R. Bonazza, *Experimental investigation of primary and secondary features in high-Mach-number shock-bubble interaction*, Phys. Rev. Lett. 98 (2007), 024502.
- [35] G.C. Orlicz, B.J. Balakumar, C.D. Tomkins, and K.P. Prestridge, *A Mach number study of the Richtmyer–Meshkov instability in a varicose, heavy-gas curtain*, Phys. Fluids 21 (2009), 064102.
- [36] E. Leinov, G. Malamud, Y. Elbaz, L.A. Levin, G. Ben-Dor, D. Shvarts, and O. Sadot, *Experimental and numerical investigation of the Richtmyer–Meshkov instability under re-shock conditions*, J. Fluid Mech. 626 (2009), p. 449.
- [37] B.J. Balakumar, G.C. Orlicz, J.R. Ristorcelli, S. Balasubramanian, K. Prestridge, and C.D. Tomkins, *Turbulence in a Richtmyer–Meshkov fluid layer after reshock: Velocity and density statistics*, J. Fluid Mech. 696 (2012), pp. 67–93.
- [38] K.A. Meyer and P.J. Blewett, *Numerical investigation of the stability of a shock-accelerated interface between two fluids*, Phys. Fluids 15 (1972), pp. 753–759.
- [39] J.W. Jacobs, D.G. Jenkins, D.L. Klein, and R.F. Benjamin, *Nonlinear growth of the shock-accelerated instability of a thin fluid layer*, J. Fluid Mech. 295 (1995), pp. 23–42.

- [40] K. Prestidge, P. Vorobieff, P.M. Rightley, and R.F. Benjamin, *Validation of an instability growth model using particle image velocimetry measurements*, Phys. Rev. Lett. 84 (2000), pp. 4353–4356.
- [41] J.G. Wouchuka and K. Nishihara, *Asymptotic growth in the linear Richtmyer–Meshkov instability*, Phys. Plasma 4 (1997), pp. 1028–1038.
- [42] J.K. Prasad, A. Rasheed, S. Kumar, and B. Sturtevant, *The late-time development of the Richtmyer–Meshkov instability*, Phys. Fluids 12 (2000), pp. 2108–2115.
- [43] B.J. Balakumar, G.C. Orlicz, C.D. Tomkins, and K. Prestidge, *Simultaneous particle-image velocimetry-planar laser-induced fluorescence measurements of Richtmyer–Meshkov instability growth in a gas curtain with and without reshock*, Phys. Fluids 20 (2008), 124103.
- [44] S. Balasubramanian, G.C. Orlicz, K.P. Prestidge, and B.J. Balakumar, *Experimental study of initial condition dependence on Richtmyer–Meshkov instability in the presence of reshock*, Phys. Fluids 24 (2012), pp. 034103–1–14.
- [45] F.F. Grinstein, L.G. Margolin, and W.J. Rider, *Implicit Large Eddy Simulation: Computing Turbulent Fluid Dynamics*, Cambridge University Press, Boston, MA, 2007.
- [46] D. Livescu and J.R. Ristorcelli, *Variable-density mixing in buoyancy-driven turbulence*, J. Fluid Mech. 605 (2008), pp. 145–180.
- [47] G. Dimonte and P. Ramaprabhu, *Simulations and model of the nonlinear Richtmyer–Meshkov instability*, Phys. Fluids 22 (2010), 014104.
- [48] M. Lombardini, D.I. Pullin, and D.I. Meiron, *Transition to turbulence in shock-driven mixing: A Mach number study*, J. Fluid Mech. 690 (2012), pp. 203–226.
- [49] S. Ukai, K. Balakrishnan, and S. Menon, *Growth rate predictions of single- and multi-mode Richtmyer–Meshkov instability with reshock*, Shock Waves 605 (2008), pp. 1–14.
- [50] O. Schilling and M. Latini, *High-order WENO simulations of three-dimensional reshocked Richtmyer–Meshkov instability to late times: Dynamics, dependence on initial conditions, and comparisons to experimental data*, Acta Math. Sci. 30 (2010), pp. 595–620.
- [51] B. Thornber, D. Drikakis, D. Youngs, and R. Williams, *The influence of initial conditions on turbulent mixing due to Richtmyer–Meshkov instability*, J. Fluid Mech. 654 (2010), pp. 99–139.
- [52] A.A. Gowardhan, J.R. Ristorcelli, and F.F. Grinstein, *The bipolar behavior of the Richtmyer–Meshkov instability*, Phys. Fluids 23 (2011), 071701.
- [53] P.E. Dimotakis, *The mixing transition in turbulent flows*, J. Fluid Mech. 409 (2000), pp. 69–98.
- [54] W. George, *Recent advancements toward the understanding of turbulent boundary layers*, AIAA J. 44 (2006), pp. 1–15.
- [55] A. Banerjee and M. Andrews, *3-D simulations to investigate initial condition effects on the growth of Rayleigh–Taylor mixing*, Int. J. Heat Mass Transfer 52 (2009), pp. 3906–3917.
- [56] P. Ramaprabhu, G. Dimonte, and M.J. Andrews, *A numerical study of the influence of initial perturbations on the turbulent Rayleigh–Taylor instability*, J. Fluid Mech. 536 (2005), pp. 285–319.
- [57] M. Hahn, D. Drikakis, D.L. Youngs, and R.J.R. Williams, *Richtmyer–Meshkov turbulent mixing arising from an inclined material interface with realistic surface perturbations and reshocked flow*, Phys. Fluids 23 (2011), 046101–046101–11.
- [58] J.W. Jacobs and J.M. Sheeley, *Experimental study of incompressible Richtmyer–Meshkov instability*, Phys. Fluids 8 (1996), pp. 405–415.
- [59] B.J. Balakumar, G.C. Orlicz, C.D. Tomkins, and K. Prestidge, *Dependence of growth patterns and mixing width on initial conditions in Richtmyer–Meshkov unstable fluid layers*, Phys. Scr. 132 (2008), 014013.
- [60] J.R. Ristorcelli and N. Hjelm, *Initial moments and parameterizing transition for Rayleigh–Taylor unstable stochastic interfaces*, J. Turbul. 11 (2010), pp. 1–27.
- [61] A.N. Kolmogorov, *The local structure of turbulence in incompressible viscous fluid for very large Reynolds numbers*, Proc. USSR Acad. Sci. 30 (1941), pp. 299–303.
- [62] A.A. Gowardhan and F.F. Grinstein, *Numerical simulation of Richtmyer–Meshkov instabilities in shocked gas curtains*, J. Turbul. 12 (2011), pp. 1–24.
- [63] S.K. Shankar and S.K. Lele, *Numerical investigation of turbulence in re-shocked Richtmyer–Meshkov unstable gas curtain of dense gas*, Shock Waves (2012), pp. 1–20.
- [64] S.B. Pope, *Turbulent Flows*, Cambridge University Press, Boston, MA, 2000.
- [65] J. Jimenez, *Intermittency and cascades*, J. Fluid Mech. 409 (2000), pp. 99–120.
- [66] D. Besnard, F. Harlow, R. Rauenzahn, and C. Zemach, *Turbulence transport equations for variable-density turbulence and their relationship to two-field models*, Tech. Rep., Los Alamos National Laboratory, 1992.

- [67] G. Dimonte and R. Tipton, *K-L turbulence model for the self-similar growth of Rayleigh–Taylor and Richtmyer–Meshkov instabilities*, Phys. Fluids 18 (2006), 085101.
- [68] A. Banerjee, R.A. Gore, and M.J. Andrews, *Development and validation of a turbulent-mix model for variable density and compressible flows*, Phys. Rev E. 82 (2010), 046309.
- [69] R.J. Adrian, *Dynamic ranges of velocity and spatial resolution of particle image velocimetry*, Meas. Sci. Technol. 8 (1997), pp. 1393–1398.

Appendix A. Error analysis

In this section, we present a brief analysis of experimental uncertainties and measurement errors associated with various turbulence quantities. In our experiments, the main sources of error are from laser intensity fluctuation, that directly affect the amplitude of the mixing layer and density measurements, the PIV processing method (e.g., optical resolution, size of interrogation window, and correlation algorithm) that affects the velocity statistics, sampling errors, and other random errors. The error and accuracy of the results presented in this paper were quantified to the extent possible.

First, we focus on the errors associated with PLIF diagnostic. The amplitude of mixing layer, δ , is directly obtained from the fluorescence signal, which is calculated from several realizations, after accounting for laser variations in the illumination intensity. The measurements of δ are estimated to be accurate to within $\pm 5\%$ based on the pixel intensity. Another quantity measured from PLIF is the density of the mixing layer, and is obtained using the mass conservation method [see 32]. This method is based on the fact that the mass of the fluorescent fluid (SF_6) is conserved inside a control volume before and after the shock, and any change in the signal is associated with the entrainment and mixing of air. Therefore, by measuring the total mass of the fluorescent fluid in the initial condition before first shock using the calibration test cell, one can calculate a scaling coefficient and use that to calculate the density of the mixing layer. The mean and fluctuating density measurements (and hence density-specific volume correlation, b) have higher statistical error, approximately $\pm 10\text{--}12\%$, due to the effects of changing laser sheet thickness that directly affects the mass calculations. Care was taken to make sure that the laser sheet thickness variation was minimal along the streamwise (x) direction.

Second, we discuss errors associated with PIV diagnostic for velocity measurements. The time response of tracer particles advected in the turbulent flow produces an error. As per [69], the estimate for the error associated with the turbulent motion of the fluid (rms particle lag, δu_{rms}) can be written as follows:

$$\delta u_{\text{rms}} \approx \frac{u^2}{\lambda_T} \left| \frac{\Delta t}{2} - \langle \tau_p \rangle \right|, \quad (\text{A1})$$

where λ_T is the Taylor microscale, Δt is the time difference between two images and τ_p is the time response of the particles. Based on $\lambda_T = 0.015$ cm, $\Delta t = 2$ μs , and $\tau_p = 0.1$ μs , we obtain an error of 0.75 $\text{m}\cdot\text{s}^{-1}$. The sub pixel error estimate is 0.1 pixel which translates to an error of 0.8 $\text{m}\cdot\text{s}^{-1}$ in the velocity fluctuation, and it is of the same order of magnitude as the error due to turbulent drag. It should be noted that the PIV vector resolution of 256 μm is approximately two times higher than the λ_T value, indicating that some statistical error is present as the flow is transitioning from large scales to smaller scales. Based on these estimates, the measurements of velocity fluctuations are accurate to within $\pm 5\%$. Some additional details on error associated with these turbulence statistics in the presence of reshock can be found in another paper published by our group [see 37].